



Prediction of (n, 2n) reaction cross-sections of long-lived fission products based on tensor model

Jia-Li Huang¹ · Hui Wang¹ · Ying-Ge Huang¹ · Er-Xi Xiao¹ · Yu-Jie Feng¹ · Xin Lei¹ · Fu-Chang Gu¹ · Long Zhu¹ · Yong-Jing Chen^{2,3} · Jun Su^{1,3}

Received: 26 March 2024 / Revised: 25 June 2024 / Accepted: 14 July 2024 / Published online: 28 September 2024

© The Author(s), under exclusive licence to China Science Publishing & Media Ltd. (Science Press), Shanghai Institute of Applied Physics, the Chinese Academy of Sciences, Chinese Nuclear Society 2024

Abstract

Interest has recently emerged in potential applications of (n, 2n) reactions of unstable nuclei. Challenges have arisen because of the scarcity of experimental cross-sectional data. This study aims to predict the (n, 2n) reaction cross-section of long-lived fission products based on a tensor model. This tensor model is an extension of the collaborative filtering algorithm used for nuclear data. It is based on tensor decomposition and completion to predict (n, 2n) reaction cross-sections; the corresponding EXFOR data are applied as training data. The reliability of the proposed tensor model was validated by comparing the calculations with data from EXFOR and different databases. Predictions were made for long-lived fission products such as ⁶⁰Co, ⁷⁹Se, ⁹³Zr, ¹⁰⁷P, ¹²⁶Sn, and ¹³⁷Cs, which provide a predicted energy range to effectively transmute long-lived fission products into shorter-lived or less radioactive isotopes. This method could be a powerful tool for completing (n, 2n) reaction cross-sectional data and shows the possibility of selective transmutation of nuclear waste.

Keywords (n, 2n) Reaction cross-section · Tensor model · Machine learning · Collaborative filtering algorithm · Selective transmutation

1 Introduction

The (n, 2n) reaction cross-sectional data are important for a wide range of applications in both fundamental and applied science. In nuclear physics, (n, 2n) reactions constitute a powerful tool for investigating the structural characteristics of excited nuclei. A prime example is the theoretical investigation of the reaction ¹⁹⁷Au(n, 2n)¹⁹⁶Au^{m2}, which is an interesting field of study because of the existence of a high-spin second metastable state [1]. In addition, the ¹⁹¹Ir (n, 2n)

reaction can help investigate the spin dependence of the level density and effective moment of inertia of residual nuclei, as well as the formation of isomeric states [2, 3]. Applied science also benefits from the (n, 2n) reaction because it can be induced by neutrons in various advanced nuclear devices such as fast reactors, thorium-based nuclear reactors, and accelerator-driven subcritical systems. These reactions are vital for neutron transport calculations. They are also indispensable for understanding the radiation damage incurred by structural materials. Consequently, achieving highly accurate evaluations of (n, 2n) reaction cross-sectional data is crucial for designing and optimizing these nuclear devices [4, 5]. Furthermore, specific (n, 2n) reactions have distinct purposes. For instance, the relative strength of ¹⁶⁹Tm(n, 2n)¹⁶⁸Tm reaction with respect to the ¹⁶⁹Tm(n, 3n)¹⁶⁷Tm reaction is a potential diagnostic tool for determining neutron flux in deuterium–tritium inertial confinement fusion plasma [6–8]. The ¹⁰⁰Mo(n, 2n)⁹⁹Mo reaction can be used to produce ^{99m}Tc, which is employed in nuclear medicine for diagnostics [9].

The cross-sectional measurements of ⁸⁶Sr(n, 2n)⁸⁵Sr provide datasets for superconductivity research in

This study was supported by the Key Laboratory of Nuclear Data foundation (No. JCKY2022201C157).

✉ Jun Su
sujun3@mail.sysu.edu.cn

¹ Sino-French Institute of Nuclear Engineering and Technology, Sun Yat-sen University, Zhuhai 519082, China

² China Nuclear Data Center, China Institute of Atomic Energy, Beijing 102413, China

³ Key Laboratory of Nuclear Data, China Institute of Atomic Energy, Beijing 102413, China

high-energy radiation zones for future fission/fusion reactor technology [10]. The $^{196}\text{Hg}(n, 2n)^{195}\text{Hg}^{\text{m,g}}$ and $^{198}\text{Hg}(n, 2n)^{197}\text{Hg}^{\text{m,g}}$ reactions are important for neutron multiplication calculations in spallation neutron sources [11]. The effective cross-sections of $^{55}\text{Mn}(n, 2n)^{54}\text{Mn}$, $^{59}\text{Co}(n, 2n)^{58}\text{Co}$, $^{176}\text{Hf}(n, 2n)^{175}\text{Hf}$, and $^{197}\text{Au}(n, 2n)^{196}\text{Au}$ reactions can help estimate fast neutron flux and energy spectrum for laser-driven neutron sources [12].

The $(n, 2n)$ reaction cross-sections of certain unstable nuclei possess exceptional significance, although measuring them is challenging owing to the limited availability and high radioactivity of high-purity materials. Notably, among the actinides, specific isotopes such as ^{241}Am (with a half-life of $T_{1/2} = 432.6$ years), ^{239}Pu ($T_{1/2} = 24,110$ years), and ^{232}Th ($T_{1/2} = 1.4 \times 10^{10}$ years) attract particular attention. The $^{241}\text{Am}(n, 2n)$ reaction cross-sections are pivotal for investigating the potential transmutation of long-lived radioactive waste, a process enabled by advanced high neutron energy reactors [13]. Similarly, the $^{239}\text{Pu}(n, 2n)^{238}\text{Pu}$ cross-sections play a critical role in estimating the production of ^{238}Pu within a fission spectrum, which is of utmost importance for evaluating the activation and decay heat characteristics of spent nuclear fuel [14]. Moreover, the $^{232}\text{Th}(n, 2n)^{231}\text{Th}$ reaction is a key factor for validating the physical design of thorium-based advanced reactors, which is a promising avenue in nuclear energy [15–17]. Despite the technical challenges of radioactive targets, significant progress has been made to overcome them. Consequently, experimental data on $(n, 2n)$ reactions involving these isotopes have been accumulated, thereby advancing our understanding of these critical nuclear processes.

In addition to reactions involving radioactive actinides, $(n, 2n)$ reactions of long-lived fission products (LLFPs) are noteworthy. Although LLFPs have shorter half-lives than radioactive actinides, the potential release of these radionuclides from geologic repositories cannot be overlooked because of their high solubility in underground water [18]. To address this problem, various transmutation strategies for LLFPs have been proposed, including irradiation with a combination of high-energy charged particles and secondary neutrons [19], and irradiation with quasi-monochromatic γ -ray beams [20]. Notably, attention has recently been directed toward the potential application of $(n, 2n)$ reactions in the transmutation of LLFPs [21]. A crucial aspect of this effort involves assessing the current status of $(n, 2n)$ cross-sectional data for LLFPs within nuclear data libraries [22]. A notable challenge has been the evaluation of cross-sections for a range of unstable nuclei across a wide energy spectrum, especially in the range where experimental data are scarce. It is worth noting that $(n, 2n)$ data for LLFPs are available for only two nuclides: ^{99}Tc and ^{129}I .

Several nuclear reaction libraries have been developed based on experimental and theoretical calculations to evaluate $(n, 2n)$ cross-sectional data [23]. Ongoing efforts are dedicated to refining the database accuracy through experimental measurements. For instance, production cross-sections for long-lived products ^{207}Bi and ^{194}Hg have been determined according to data measured by an ultralow background gamma spectrometer (GeTHU) in the China Jinping Underground Laboratory (CJPL) [24]. A new 4π neutron detector was constructed to minimize the background γ -ray influence and improve the $(n, 2n)$ reaction cross-sectional measurements [25]. However, unique challenges arise from the short lifetimes or high radioactivity of the target materials, rendering direct measurements of $(n, 2n)$ cross-sections for radioactive nuclides unattainable using current experimental techniques. Indirect methods are being developed to address this challenge [26]. Given the current circumstances, extrapolation from databases using physics-based models [27] or statistical algorithms [28] remains both advisable and effective. This approach helps bridge the gap in our understanding of $(n, 2n)$ reactions involving unstable nuclides.

The extensive application of machine learning in nuclear physics has introduced new ideas into nuclear data evaluation. Machine learning has been successfully employed in various research fields, such as nuclear charge radius [29], nuclear mass [30–32], fission cross-sections [33], fragmentation reactions [34, 35], and nuclear equation of state [36–38]. Machine learning facilitates data evaluation [39], validation analysis [40], and prediction [41]. For instance, Bayesian neural networks have proven successful in predicting $(n, 2n)$ reaction cross-sections [42]. Collaborative filtering is a machine learning technique used in recommendation systems to automatically predict the interests of a user. It has been extended to the field of nuclear data, developing into a tensor model for evaluating fission product yields [43, 44] and differential cross-sections for elastic proton scattering [45]. In this study, the applicability of a tensor model for evaluating the EXFOR data of $(n, 2n)$ reaction cross-sections was investigated. The objective is to predict the $(n, 2n)$ reaction cross-section of long-lived fission products.

The remainder of this paper is organized as follows. Section 2 provides a detailed description of the constructed tensor model. In Sect. 3, we validate the reliability of the model and explore its application to selective transmutations. The reproductive ability of the model was assessed in cases with abundant and scarce experimental data. Detailed examples are provided to explain the collaborative filtering algorithm. Overall reproduction results are also presented. Predictions were made in the absence of abundant training data and data featuring significant deviations. The predictions of the cross-sections of long-lived

fission products are analyzed. Finally, Sect. 4 concludes the paper and discusses future prospects.

2 Theoretical descriptions

The proposed tensor model is an extension of the collaborative filtering algorithm employed in the field of nuclear data. The core algorithm is based on tensor decomposition and completion. The tensor decomposition algorithm is a machine learning algorithm with powerful multi-dimensional structure correlation learning capabilities. This algorithm has found widespread application in fields such as image processing and data mining [46–48]. The Bayesian model was introduced in the field of matrix completion by Salakhutdinov and Mnih, who developed Bayesian matrix factorization models [49]. Xiong et al. combined Bayesian inference and tensor decomposition, considering the time dependency of each tensor [50]. Chen et al. further improved the Bayesian Gaussian CANDECOMP/PARAFAC (BGCP) tensor decomposition model without considering the time structure [51]. Subsequently, Wang et al. extended the Bayesian tensor decomposition approach and studied cross-sections in neutron-induced threshold (n, 2n) and photoneutron (γ, xn) reactions by constructing weighted evolving networks [52].

The (n, 2n) cross-section depends on three degrees of freedom: proton number, isospin number, and incident energy of the neutron. To represent the threshold effect, the following reduced incident energy is applied:

$$E = \frac{A}{A + 1} E_n - S_n, \tag{1}$$

where A is the mass of the target, E_n is the incident energy of the laboratory system, and S_n is the single-neutron separation energy of the target. The (n, 2n) reaction occurs only when $E > 0$. After discretizing the reduced energy E with the interval $dE = 0.5$ MeV, the (n, 2n) cross-sectional data can be expressed as a third-order tensor denoted as $\mathcal{S} \in \mathbb{R}^{I \times J \times K}$, where the element σ_{ijk} is the (n,2n) cross-section for the target with charge number i and neutron number $i+j$ at reduced incident energy $k \times dE$. With the experimental data obtained from the EXFOR database, some elements are observed, while others are missing. In this case, the missing tensor of the (n, 2n) cross-section is complemented using a machine learning algorithm called the BGCP tensor decomposition algorithm. Reference [47] provides a detailed introduction to the BGCP algorithm. Here, we briefly introduce how BGCP has been applied in this study.

The tensor is estimated using the factor matrices $\mathbf{Z} \in \mathbb{R}^{I \times L}$, $\mathbf{D} \in \mathbb{R}^{J \times L}$, and $\mathbf{E} \in \mathbb{R}^{K \times L}$:

$$\hat{\mathcal{S}} = \sum_{l=1}^L z_l \circ d_l \circ e_l, \tag{2}$$

where L is the CANDECOMP/PARAFAC (CP) rank, $z_l \in \mathbb{R}^I$, $d_l \in \mathbb{R}^J$, and $e_l \in \mathbb{R}^K$ are, respectively, the l -th column vector of the factor matrices \mathbf{Z} , \mathbf{D} , and \mathbf{E} . The symbol \circ denotes the outer product of the vector. Equation (2) can be specifically expressed as

$$\hat{\sigma}_{ijk} = \sum_{l=1}^L z_{il} \circ d_{jl} \circ e_{kl}, \tag{3}$$

where z_{il} is the element at the i -th row and l -th column in the factor matrix \mathbf{Z} ; d_{jl} and e_{kl} are similar.

To model the tensor data correctly, the factor matrices \mathbf{Z} , \mathbf{D} , and \mathbf{E} are set with prior distributions. We assume that the prior distributions over the row vectors of each factor matrix obey multi-variate Gaussian distributions. Consider the i -th row vector of \mathbf{Z} as an example. The other cases are similar. The elements in the factor matrix \mathbf{Z} are expressed as random variables:

$$z_i \sim \mathcal{N} \left[\boldsymbol{\mu}_i^{(z)}, (\boldsymbol{\Lambda}_i^{(z)})^{-1} \right], \tag{4}$$

where the hyper-parameter $\boldsymbol{\mu}^{(z)} \in \mathbb{R}^L$ represents the expectation, and $\boldsymbol{\Lambda}^{(z)} \in \mathbb{R}^{L \times L}$ represents the reciprocal of the standard deviation.

The observation of the tensor element σ_{ijk} is considered a random variable. We assume that each observation follows an independent Gaussian distribution:

$$\sigma_{ijk} \sim \mathcal{N}(\hat{\sigma}_{ijk}, \tau_\epsilon^{-1}), \tag{5}$$

where $(i, j, k) \in \mathbf{Q}$; τ_ϵ is the precision, which expresses the reciprocal of the discrepancy between measurements; and \mathbf{Q} is the index set of observations. The factor matrix \mathbf{Z} is updated by sampling all z_i individually. After updating \mathbf{Z} , \mathbf{D} , and \mathbf{E} , which are explained in detail later, $\hat{\sigma}_{ijk}$ is also updated. Subsequently, the random variable σ_{ijk} is updated using Eq. (5), thereby providing a prediction for the next measurement.

Considering multiple measurements, let $\sigma_{ijk}^{(p)}$ ($p = 1, \dots, P_{ijk}$) represent the p -th observation of the cross-section for a total of P_{ijk} observations. It should be noted that the tensor \mathcal{S} is incomplete, presenting missing entries. A list of missing tensors $\tilde{\mathcal{S}} = \{\mathcal{S}^{(1)}, \dots, \mathcal{S}^{(P)}\}$ can be used to describe all observations, where $P = \max(P_{ijk})$ for all possible ijk . The observations are arranged in the missing tensors according to their superscripts, e.g., $\sigma_{ijk}^{(1)}$ in $\mathcal{S}^{(1)}$ and $\sigma_{ijk}^{(2)}$ in $\mathcal{S}^{(2)}$. Entries with no observations are missing.

The likelihood function can be expressed as follows:

$$\mathcal{L}(\sigma_{ijk}^{(p)} | z_i, \mathbf{d}_j, \mathbf{e}_k, \tau_\epsilon) \propto \exp \left\{ -\frac{\tau_\epsilon}{2} [\sigma_{ijk}^{(p)} - (z_i)^T (\mathbf{d}_j \otimes \mathbf{e}_k)]^2 \right\}, \quad (6)$$

where \otimes denotes the Hadamard product.

Subsequently, according to Bayesian inference, the posterior distribution of z_i can be expressed as follows:

$$p(z_i | \sigma_{ijk}^{(p)}, \mathbf{d}_j, \mathbf{e}_k, \tau_\epsilon, \boldsymbol{\mu}^{(z)}, \boldsymbol{\Lambda}^{(z)}) \propto L(\sigma_{ijk}^{(p)} | z_i, \mathbf{d}_j, \mathbf{e}_k, \tau_\epsilon) \times Pr(z_i) \propto \mathcal{N}(z_i | (\hat{\boldsymbol{\mu}}_i^{(z)}, (\hat{\boldsymbol{\Lambda}}_i^{(z)})^{-1})) \quad (7)$$

where the posterior values of the hyper-parameters $\boldsymbol{\mu}^{(z)}$ and $\boldsymbol{\Lambda}^{(z)}$ are given by

$$\begin{aligned} \hat{\boldsymbol{\Lambda}}_i^{(z)} &= \tau_\epsilon (\mathbf{d}_j \otimes \mathbf{e}_k) (\mathbf{d}_j \otimes \mathbf{e}_k)^T + \boldsymbol{\Lambda}_i^{(z)}, \\ \hat{\boldsymbol{\mu}}_i^{(z)} &= (\hat{\boldsymbol{\Lambda}}_i^{(z)})^{-1} \left[\tau_\epsilon \sigma_{ijk}^{(p)} (\mathbf{d}_j \otimes \mathbf{e}_k) + \boldsymbol{\Lambda}_i^{(z)} \boldsymbol{\mu}_i^{(z)} \right]. \end{aligned} \quad (8)$$

The contributions of the observations to the hyper-parameters are equivalent, being independent of the missing tensor. The likelihood function of all the observations is

$$\mathcal{L}(\tilde{\mathcal{S}} | \mathbf{Z}, \mathbf{D}, \mathbf{E}, \tau_\epsilon) \propto \prod_{p=1}^P \prod_{i=1}^I \prod_{j=1}^J \prod_{k=1}^K (\tau_\epsilon)^{1/2} \exp \left[-\frac{\tau_\epsilon}{2} b_{ijk}^{(p)} (\sigma_{ijk}^{(p)} - \bar{\sigma}_{ijk})^2 \right], \quad (9)$$

where $\bar{\sigma}_{ijk}$ denotes the average value of the cross-section after several experimental measurements, and $b_{ijk}^{(p)}$ is equal to 1 for measured entries and 0 for missing entries. Let us place a conjugate Γ prior to the precision τ_ϵ :

$$\tau_\epsilon \sim \Gamma(a_0, b_0), \quad (10)$$

where the posterior values of the hyper-parameters a_0 and b_0 are given by

$$\begin{aligned} \hat{a}_0 &= \frac{1}{2} \sum_{p=1}^P \sum_{i=1}^I \sum_{j=1}^J \sum_{k=1}^K b_{ijk}^{(p)} + a_0, \\ \hat{b}_0 &= \frac{1}{2} \sum_{p=1}^P \sum_{i=1}^I \sum_{j=1}^J \sum_{k=1}^K (\sigma_{ijk}^{(p)} - \bar{\sigma}_{ijk})^2 + b_0. \end{aligned} \quad (11)$$

Figure 1 shows the iterative steps of the tensor model. The cross-section of a specific nuclide is represented as $\hat{\mathcal{S}}$. Using CP decomposition, we express the tensor $\hat{\mathcal{S}}$ as the outer product of three factor matrices, i.e., \mathbf{Z} , \mathbf{D} , and \mathbf{E} , corresponding to the three dimensions mentioned earlier. We assume that the prior distributions for the factor matrices are multi-variate Gaussians. The likelihood function is derived from observed data. The posterior distributions of the hyper-parameters and the precision are updated. Subsequently, the posterior distributions of \mathbf{Z} , \mathbf{D} , and \mathbf{E} are obtained through Bayesian inference. Each iteration updates all the variables sequentially using Gibbs sampling. The relationship between each parameter and the observed value is captured using data sampling. The iterations continue until the precision reaches its optimal level. Upon reconstructing the tensor $\hat{\mathcal{S}}$ with the updated values, we obtain the complete cross-sectional tensor.

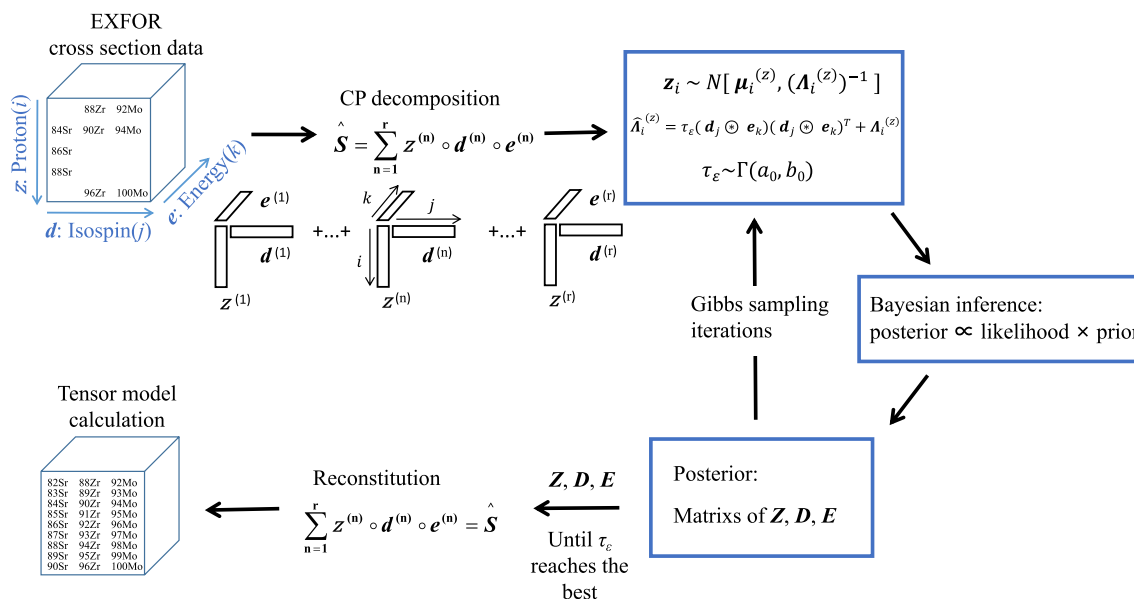


Fig. 1 (Color online) Model framework presentation

3 Results and discussion

3.1 Model validation

Figure 2 displays the (n, 2n) cross-sections for the isotopes of Co, Cu, Ga, Se, Zr, Tc, Pd, Sn, Sb, I, Xe, Cs, Sm, Hf, Pb, and Bi. They can be classified into two types: cases where the experimental data are abundant and cases where the data are scarce. Except for ⁸⁸Zr and ⁹⁹Tc, the available data for these nuclides are abundant. As the incident energy increases above the threshold, the cross-section experiences a rapid increase, reaching barn-level magnitudes. The threshold energy for the reaction ^AX(n, 2n)^{A-1}X corresponds to the single-neutron separation energy of ^AX. Above 16 MeV, the cross-section exhibits a slight decrease. The curves in the figures represent calculations performed using the proposed tensor model; they are generally consistent with the available data.

3.1.1 Cases with abundant experimental data

Cases with abundant experimental data are further classified according to discrepancies within the data. Tensor models rely on data-driven approaches. The combination of extensive data support and a tensor decomposition algorithm ensures the reliability of our calculations. In cases where abundant data points concentrate on the overall trend, as exemplified by the case of ⁶³Cu shown in Fig. 2b, our calculations closely approximate the average of the data, resulting in smooth curves. Similar results are observed in Fig. 2e for ⁹⁰Zr.

In some cases, there are limited outliers, such as those shown in Fig. 2b for ⁶⁵Cu. Limited data points, some of which deviate from the overall trend, are indicated by circles. Although considered as low-quality data, these outliers do not impede the model to perform well, and the calculated results for ⁶⁵Cu remain smooth. Figure 2c presents a scenario with even fewer data points and a relatively large proportion of low-quality data. However, the tensor model is still characterized by smooth calculations. This pattern holds for ⁸²Se

Fig. 2 (Color online) (n, 2n) cross-sections for isotopes of Co, Cu, Ga, Se, Zr, Tc, Pd, Sn, Sb, I, Xe, Cs, Sm, Hf, Pb, and Bi. The curves show the calculations by the tensor model, whereas the dots represent the EXFOR data

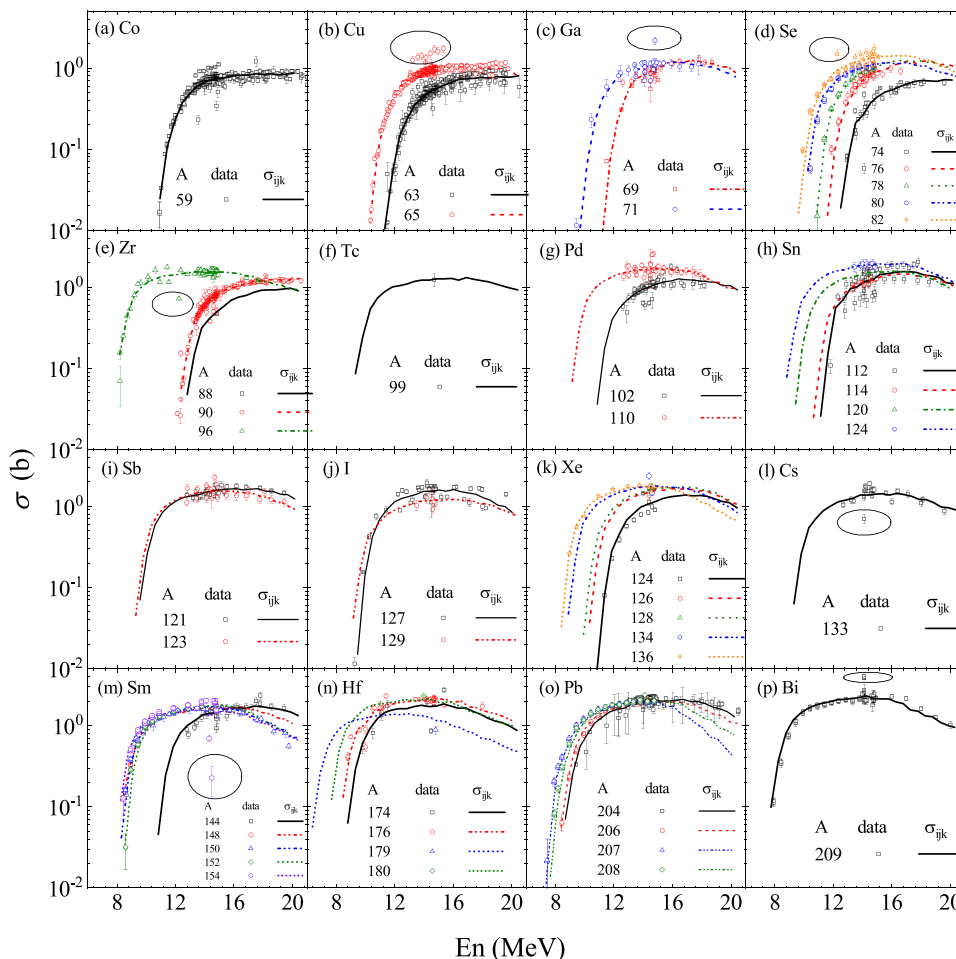


(Fig. 2d), ^{96}Zr (Fig. 2e), ^{133}Cs (Fig. 2l), ^{154}Sm (Fig. 2m), and ^{209}Bi (Fig. 2p), respectively.

In the other cases, there are large deviations within the data. For example, for ^{127}I (Fig. 2j), noticeable data discrepancies are observed within the same energy region. Despite these variations, the proposed tensor model maintains its ability to generate calculations within the range of the available data. This robust quality control is also evident for ^{112}Sn (Fig. 2h) and ^{174}Hf (Fig. 2n). The tensor model effectively addresses the challenge of data quality dependence, ensuring reliable results even in the case of ‘high quantity but low quality’ data. Small oscillatory behaviors are observed in these cases, which may be attributed to hidden errors within the experimental data.

This oscillatory behavior is also observed in Fig. 2k for ^{124}Xe . In this case, the calculations near 14 MeV exceed the observed data. This deviation may also be attributed to hidden errors in the experimental data. Typically, data are published with both systematic and statistical errors, which are visually represented as error bars in the figures. However, in certain cases, the error bars may not reflect the deviation of the observed data from other measurements. These errors can be concealed, particularly when comparable data are scarce. They could stem from factors related to the measurement instruments or data analysis processes. The unexpected calculations for ^{124}Xe suggest the presence of potential hidden errors in the corresponding data. A more comprehensive evaluation is necessary with reference to an evaluation database and a physical model.

3.1.2 Cases with scarce experimental data

For cases where experimental data are scarce, ^{99}Tc (Fig. 2f) is taken as an example. Note that in Fig. 2f, only one data point is observed for ^{99}Tc . The cross-sections as a function of the incident energy were calculated using the tensor model, exhibiting a reasonable trend. As described in Eq. (3), these calculations at a given incident energy ($E_k = k \times dE$, for example) for ^{99}Tc are derived not only from the data for ^{99}Tc but also from the data for ^{103}Rh and data at energy E_k for all nuclei. The $N-Z$ value of ^{103}Rh matches that of ^{99}Tc ; further details are illustrated in Fig. 3.

3.1.3 Detailed examples of the collaborative filtering algorithm

Figure 3 displays the $(n, 2n)$ cross-sections for isotopes of Cu, Ga, Tc, and Rh. To validate the calculations performed using the proposed tensor model, we compare them with experimental data for ^{65}Cu and ^{99}Tc , as illustrated in Fig. 3a and c. The comparison involves data from various databases, including ENDF/B-VIII.0, JENDL-5, JEFF-3.3,

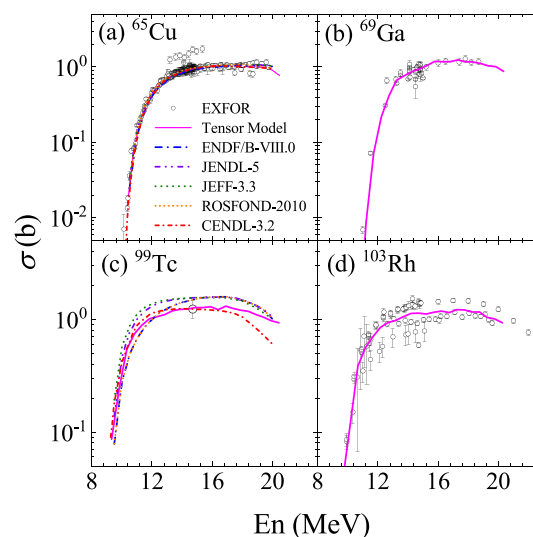


Fig. 3 (Color online) $(n, 2n)$ cross-sections for isotopes of Cu, Ga, Tc, and Rh. The solid curves represent calculations by the tensor model, the dotted curves represent data from databases ENDF/B-VIII.0, JENDL-5, JEFF-3.3, ROSFOND-2010, and CENDL-3.2, and the dots represent EXFOR data

ROSFOND-2010, and CENDL-3.2; all of them exhibit similar trends to those of the EXFOR data. The solid curves in the figures represent calculations generated by the proposed tensor model. Overall, these calculations are consistent with the data obtained from the aforementioned databases. To shed light on the impact of collaborative filtering, Fig. 3b and d presents the cross-sections of ^{69}Ga and ^{103}Rh , respectively. Notably, these nuclides feature the same isospin values as those of ^{65}Cu and ^{99}Tc .

The tensor model is based on collaborative filtering, which is a formula-free fitting method described by Eq. (3). Calculations at specific incident energies for a given nuclide are drawn not only from its own data but also from data associated with the same isospin (same $N-Z$ value), isotopes (same Z value), and data at that energy for all nuclei. We consider the case of ^{65}Cu shown in Fig. 3a. Data from various databases, excluding EXFOR, generally exhibit good agreement with each other, featuring small deviations. Even for the EXFOR data, which served as training data for the model, a minority of the data points deviates from the overall trend. Importantly, these outliers do not adversely affect the quality of the calculations. This is evident from the completion of the excitation function for $^{65}\text{Cu}(n, 2n)^{64}\text{Cu}$, where the model captures reasonable physical laws. Consequently, the calculations for ^{65}Cu remain smooth and are consistent with data from ENDF/B-VIII.0, JENDL-5, JEFF-3.3, ROSFOND-2010, and CENDL-3.2. It is worth noting that calculations for ^{65}Cu were also drawn from the data for ^{69}Ga , as shown in Fig. 3b. In this figure, it is evident that a substantial and

dense dataset spanning the energy range from 13 MeV to 15 MeV significantly influences the calculations for ⁶⁹Ga and ⁶⁵Cu in this energy region.

For ⁹⁹Tc (Fig. 3c), the data from various databases deviate from each other across all energy ranges. In contrast, the calculations produced by the tensor model exhibit a reasonable trend. Notably, the solid curve representing the calculations is based on a single data point from EXFOR. These calculations for ⁹⁹Tc are influenced not only by the data for ⁹⁹Tc but also by the data for ¹⁰³Rh, as shown in Fig. 3d. Figure 3d shows that the data for ¹⁰³Rh are abundant but exhibit substantial deviations. However, the calculations using the tensor model remain smooth and fall within the range of the available data. Above 16 MeV, the calculations for ⁹⁹Tc are influenced by the data for ¹⁰³Rh in this energy region, resulting in a slight decrease in the cross-section. This collective approach allows the completion of the excitation function for ⁹⁹Tc(n, 2n)⁹⁸Tc using these data. The algorithm of the tensor model ensures the reliability of these calculations.

3.1.4 Overall results of the reproduction

Figure 4 provides statistical information on 5770 EXFOR data points within the energy region from 0 to 20 MeV. In Fig. 4a, we observe the ratios between the model calculations and the data. These ratios exhibit global variation within the range from 0.1 to 10, with a predominant concentration around 1. Ratios exceeding 1 indicate an overestimation by the model, whereas those below 1 represent an underestimation. Notably, the maximum ratio can reach magnitudes of 10³. At energy levels below 15 MeV, the deviations in these ratios can reach a factor of 10⁴,

whereas they are approximately limited to a factor of 10 at energy levels above 15 MeV. The region around 14 MeV seems to contain a dense cluster of data points.

Figure 4b represents the quantity of data as a function of energy, with data counts calculated for each 0.5 MeV interval. Notably, there is a substantial concentration of data in the energy range from 13 to 15 MeV, with the maximum count reaching 1800 data points. Obtaining data for neutrons near 14 MeV seems to be more accessible than for other energy ranges. By contrast, the number of data points in other energy regions remains relatively low, with no more than 300 data points in each interval. It is important to note that extensive support from this wealth of data can significantly enhance the reliability of the calculations performed using the tensor model.

Figure 4c shows the relative errors associated with the data. Typically, data are accompanied by both systematic and statistical errors, which are represented as error bars in the figures. The relative errors shown in Fig. 4c are defined as $\Delta\sigma/\sigma$. These relative errors range from 10⁻³ to 10. In the energy region below 15 MeV, the relative errors are particularly large, whereas in the energy region above 15 MeV, the relative errors are generally smaller, not exceeding 10. Notably, the presence of these larger relative errors may have contributed to the substantial deviations observed in the ratios shown in Fig. 4a.

Figure 5 presents a detailed examination of the ratios using a logarithmic scale and the corresponding proportions. Figure 5a shows the logarithms of the ratios between the model calculations and the data for energy ranging from 0 to 40 MeV. This representation simplifies the comparison of orders of magnitude. Notably, the logarithmic errors primarily range from -0.1 to 0.1. In practical terms, this implies that the ratios typically range from 10^{-0.1} to 10^{0.1},

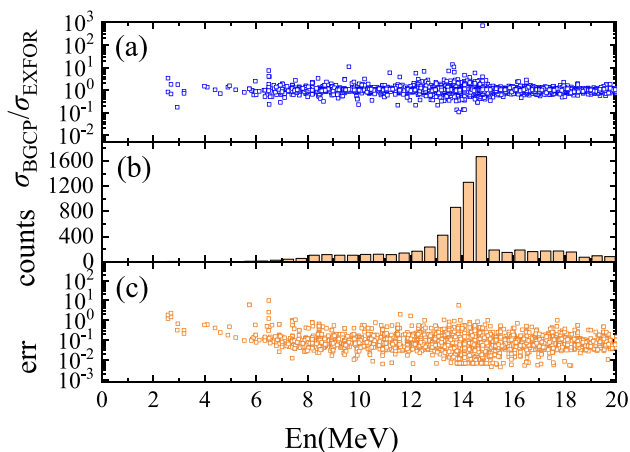


Fig. 4 (Color online) Statistic information of 5770 EXFOR data in the range from 0 to 20 MeV in the laboratory: **a** ratios between calculations and the data; **b** energy distribution of the data; and **c** relative errors

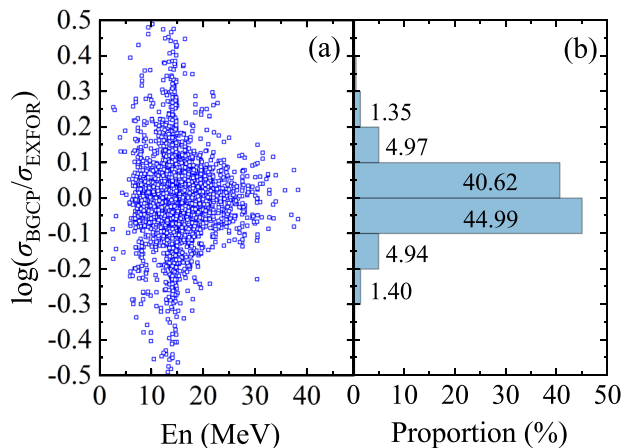


Fig. 5 (Color online) Logarithm of the ratios between the calculations and data (logarithmic error): **a** energy distribution of the logarithmic errors and **b** count of errors of different sizes

corresponding to values between 0.79 and 1.25. The corresponding ratios are shown in Fig. 5b, where 44.99% of the data points exhibit logarithmic errors between 0.0 and -0.1 , and 40.62% display logarithmic errors between 0.0 and 0.1. Notably, logarithmic errors within the range from -0.3 to 0.3, equivalent to ratios between 0.5 and 2.0, indicate deviations between the calculations and the data less than a factor of 2; the corresponding proportion exceeds 90%.

3.1.5 Prediction in the absence of abundant training data

The discussion thus far has primarily focused on validating the reproductive ability of the model. The model has demonstrated its capacity to complete the excitation functions using data from the training dataset. The next step involves assessing the prediction ability of the model, specifically its capability to predict cross-sections and complete excitation functions for nuclides that lack data in the training dataset. This is a crucial aspect in evaluating the generalization ability of the model and its predictive power. Two conditions are considered to assess the prediction ability of the model: Predictions are made in the absence of training data, which are abundant, and have significant deviations.

Figure 6 presents the $(n, 2n)$ cross-sections for ^{90}Zr and its isotopes, ^{88}Zr and ^{96}Zr . This case was designed to assess the predictive ability of the model in the absence of training data. In Fig. 6a, we distinguish between calculations labeled as reproductions and predictions. It is important to note that a wealth of data are available for ^{90}Zr . The reproductions were generated by the tensor model trained using the dataset that includes ^{90}Zr data, whereas the predictions were obtained using the same model without incorporating any ^{90}Zr data during the training process. Both the reproduction and prediction results exhibit global consistency with the EXFOR data. Despite the absence of training data, the model predictions for ^{90}Zr are remarkably consistent with the data. The deviation between the calculations with and without the inclusion of ^{90}Zr data remains small.

Figure 6b shows the cross-sections for ^{90}Zr , both calculated by the tensor model and obtained from various databases, including BROND-3.1, CENDL-3.2, ENDF/B-VII.1, JEFF-3.3, JENDL-4.0, and TENDL-2019. These datasets exhibit consistent trends, with small deviations between the data represented by the dotted curves. The predictions provided by the tensor model (depicted as a solid curve) are consistent with the data.

Figure 6c shows the cross-sections of ^{88}Zr and ^{96}Zr . For ^{96}Zr , similar to the example shown in Fig. 2b, several data points deviate significantly from the overall trend. However, these deviations do not lead to poor model calculations for ^{96}Zr . The situation for ^{88}Zr resembles that of ^{99}Tc , as shown in Fig. 2f, where a single data point is available. The

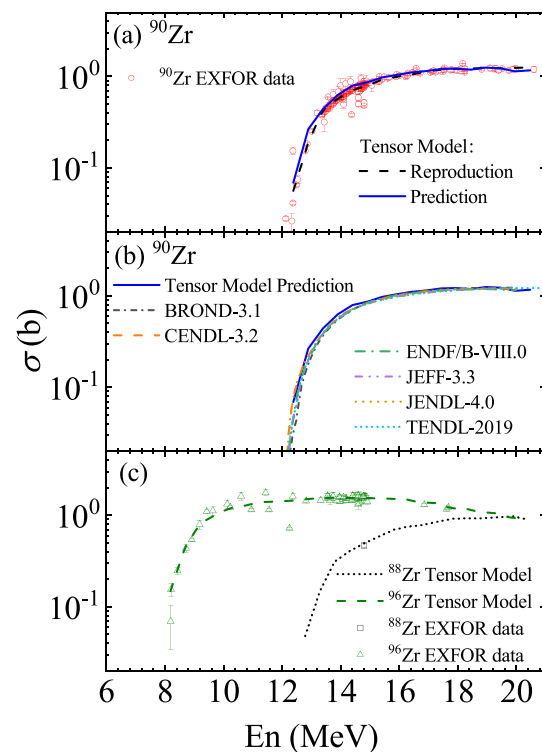


Fig. 6 (Color online) $(n, 2n)$ cross-sections for ^{90}Zr and its isotopes ^{88}Zr and ^{96}Zr . The calculation labeled as reproduction was generated by the tensor model trained using the dataset that includes ^{90}Zr data, while the calculation labeled as prediction was obtained using the same model without incorporating any ^{90}Zr data during the training process

excitation function of $^{88}\text{Zr}(n, 2n)^{87}\text{Zr}$ can still be determined. The cross-sections for ^{88}Zr and ^{96}Zr significantly contribute to the predictions for ^{90}Zr . Therefore, the excitation function of $^{90}\text{Zr}(n, 2n)^{89}\text{Zr}$ can be accurately obtained without utilizing the data specifically for ^{90}Zr .

3.1.6 Prediction in the absence of data with significant deviations

Figure 7 shows the $(n, 2n)$ cross-sections for ^{84}Sr and its isotopes ^{86}Sr and ^{88}Sr . This case tests the prediction ability of the model in the absence of a set of training data exhibiting large deviations. For ^{84}Sr (Fig. 7a), the deviation in the data is large. The error bars do not cover the deviation from other data. The reproductions by the tensor model, indicated by the dotted curve in the figure, exhibit large numerical fluctuations. The abnormal calculations for ^{84}Sr may indicate hidden errors in the corresponding data. The predictions are represented by solid curves in Fig. 7a. Note that the missing data do not generate bad predictions. The predictions for ^{84}Sr were derived from its isotopes and are smoother. This

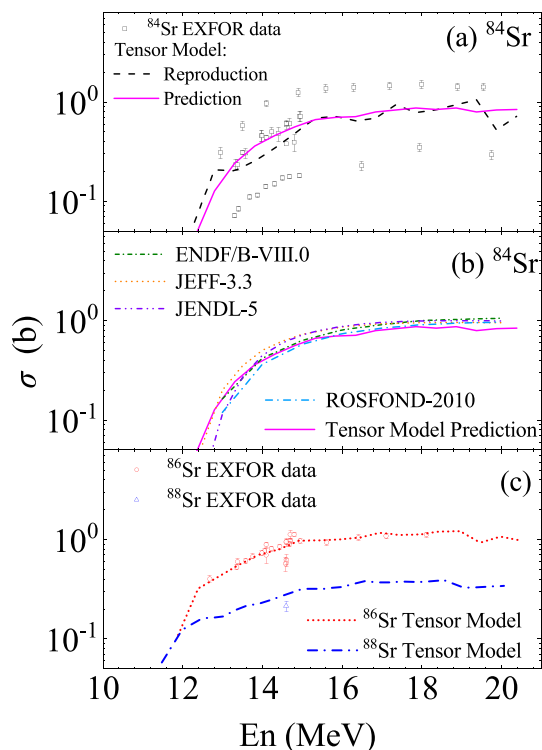


Fig. 7 (Color online) (n, 2n) cross-sections for ^{84}Sr and its isotopes ^{86}Sr and ^{88}Sr

Figure 7b shows the cross-sections for ^{84}Sr from the tensor model and from databases ENDF/B-VIII.0, JEFF-3.3, JENDL-5, and ROSFOND-2010. As indicated by the dotted curves, the data trends are similar, but there exist deviations. The predictions of the model are consistent with the data in the energy region below 15 MeV. The tensor model underestimates the cross-sections in the energy region above 15 MeV.

Figure 7c shows the cross-sections for ^{86}Sr and ^{88}Sr . The case of ^{86}Sr is similar to that of ^{96}Zr , as shown in Fig. 6c. However, there are numerical fluctuations in the energy region above 18 MeV. The behavior of ^{88}Sr is similar to that of ^{88}Zr . The cross-sections increase rapidly and then begin to decrease, which is a reasonable trend. The curve does not pass through the data point but is close. There are also numerical fluctuations in the calculations at 13 MeV and 19 MeV. The collaborative filtering algorithm of the model helps complete the excitation; however, this is also the reason for the small numerical fluctuations in the calculations for both ^{86}Sr and ^{88}Sr . The cross-sections for ^{86}Sr and ^{88}Sr contribute to the predictions for ^{84}Sr . The excitation function of $^{84}\text{Sr}(n, 2n)^{83}\text{Sr}$ can be completed, and the predictions are smooth. This also indicates that further improvements are required with the help of the evaluation database and physical model to reduce hidden errors.

is also attributed to the contributions of the data associated with the same isospin value and the data in its energy region for all nuclei.

Fig. 8 (Color online) (n, 2n) cross-sections for ^{60}Co , ^{79}Se , ^{93}Zr , ^{107}Pd , ^{126}Sn , and ^{137}Cs . The solid curves represent the calculations by the tensor model, whereas the dotted curves represent the data from databases CENDL-3.2, ENDF/B-VIII.0, JEFF-3.3, JENDL-4.0, and TENDL-2019

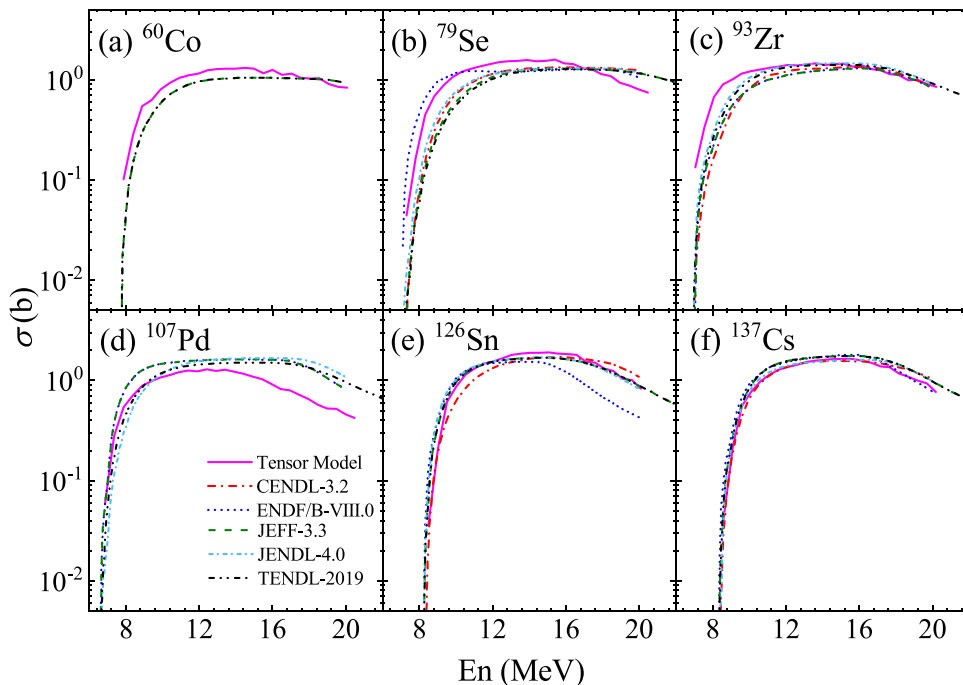


Table 1 Training data for ^{60}Co , ^{79}Se , ^{93}Zr , ^{107}Pd , ^{126}Sn , and ^{137}Cs

Nuclide	^{60}Co	^{79}Se	^{93}Zr	^{107}Pd	^{126}Sn	^{137}Cs
Same Z	^{59}Co	$^{74,76,78,80,82}\text{Se}$	$^{88,90,96}\text{Zr}$	$^{102,110}\text{Pd}$	$^{112,114,120,124}\text{Sn}$	^{133}Cs
Amount	280	149	262	93	72	24
Same N-Z	$^{66}\text{Zn}, ^{74}\text{Se}$ $^{70}\text{Ge}, ^{78}\text{Kr}$	$^{81}\text{Br}, ^{85}\text{Rb}$ $^{89}\text{Y}, ^{93}\text{Nb}$	$^{87}\text{Rb}, ^{99}\text{Tc}$ $^{103}\text{Rh}, ^{107}\text{Ag}$	^{109}Ag ^{113}In	$^{130}\text{Te}, ^{134}\text{Xe}, ^{138}\text{Ba}$ $^{142}\text{Ce}, ^{146}\text{Nd}, ^{150}\text{Sm}$ $^{154}\text{Gd}, ^{158}\text{Dy}, ^{162}\text{Er}$	$^{153}\text{Eu}, ^{155}\text{Gd}$
Amount	150	343	142	77	249	51
Sum	430	492	404	170	321	75

3.1.7 Prediction of cross-sections of long-lived fission products

Figure 8 provides a comprehensive overview of the (n, 2n) cross-sections for long-lived fission products, including ^{60}Co ($T_{1/2} = 5$ years), ^{79}Se ($T_{1/2} = 32$ years), ^{93}Zr ($T_{1/2} = 1.59 \times 10^6$ years), ^{107}Pd ($T_{1/2} = 6.33 \times 10^6$ years), ^{126}Sn ($T_{1/2} = 23$ years), and ^{137}Cs ($T_{1/2} = 30$ years). These nuclides are radioactive and play a significant role in the study of fission products. Note that there are no EXFOR data available for these specific nuclides. As such, we compared the calculations with data from other databases, which sometimes exhibit deviations among themselves. However, the calculations generated by the proposed tensor model, represented by the solid curves in the figures, demonstrate consistent and strong global agreement with the data.

The proposed tensor model exhibits capability to complete excitation functions even in the absence of specific data. The model also demonstrates strong predictive abilities, consistently aligning with data from various databases. To illustrate this, let us consider the example of ^{126}Sn in Fig. 8e. While deviations are noticeable among the data from various databases, especially in the energy regions below 14 MeV and above 15 MeV, the calculations of the model maintain robust global agreement with the data, excluding those from ENDF/B-VIII.0.

For ^{137}Cs (Fig. 8f), small deviations are observed among the data from various databases, primarily in the energy region above 10 MeV. However, the model calculations consistently align with the data from CENDL-3.2 and JENDL-4.0 below 18 MeV. Furthermore, the model agrees with the data from ENDF/B-VIII.0, particularly near 19 MeV.

For ^{60}Co (Fig. 8a), the data from JEFF-3.3 and TENDL-2019 are consistent. However, the tensor model demonstrates a trend of overestimating the cross-sections below 18 MeV and underestimating them above 19 MeV.

In the case of ^{79}Se (Fig. 8b), deviations among the data from various databases are apparent, particularly in the energy region below 12 MeV. The tensor model generally overestimates the cross-sections between 10 MeV and 16 MeV and underestimates them above 17 MeV.

For ^{93}Zr (Fig. 8c), deviations are noticeable in the data from various databases, particularly in the energy region above 8 MeV. The tensor model tends to overestimate cross-sections below 11 MeV.

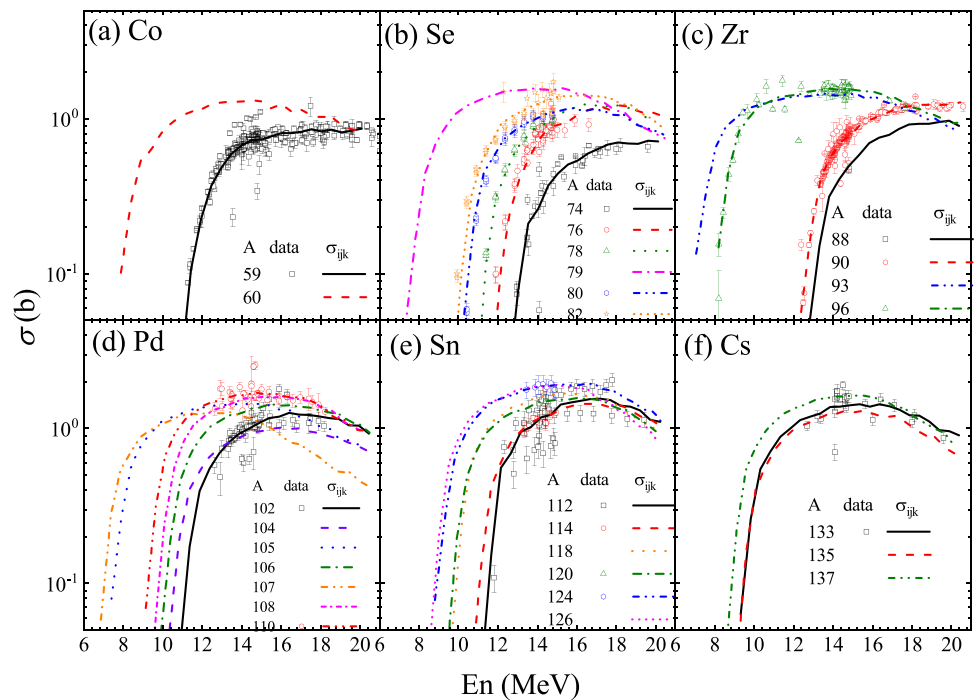
However, there is notable agreement between the model calculations and data from databases such as JENDL-4.0 and TENDL-2019 in the range from 11 to 16 MeV. Moreover, the model aligns with the data from ENDF/B-VIII.0 and JEFF-3.3 above 16 MeV. Although deviations between the calculations and data exist, they remain within an order of magnitude.

For ^{107}Pd (Fig. 8d), deviations in the data become evident, particularly in the energy regions below 12 MeV and above 18 MeV. Notably, the model calculations are consistent with data from databases such as JEFF-3.3 and ENDF/B-VIII.0 below 7 MeV. However, above 10 MeV, the tensor model tends to underestimate the cross-sections, with a rapid decrease. A similar decreasing trend is observed in the data from ENDF/B-VIII.0 shown in Fig. 8e.

To further determine the manner in which the tensor model completes the excitation functions in Fig. 8, Table 1 summarizes the nuclides applied in the calculations and their corresponding amounts. This table lists the training data for ^{60}Co , ^{79}Se , ^{93}Zr , ^{107}Pd , ^{126}Sn , and ^{137}Cs . The energy region ranges from 0 to 20 MeV. This is the same contribution from the data for all nuclides at the same energy. Therefore, the focus is particularly put on the data of nuclides that have the same proton number Z or isospins $N-Z$ as the target nucleus. By contrast, the total quantities of training data for ^{60}Co , ^{79}Se , ^{93}Zr , ^{107}Pd , and ^{126}Sn are larger than those for ^{137}Cs . However, as shown in Fig. 8, the calculations for ^{137}Cs are more precise. This indicates that the amount of training data may not be the predominant factor influencing model calculations.

Taking ^{137}Cs and ^{107}Pd as examples, for isotopes with the same proton number as ^{137}Cs ($Z = 55$), only the data for ^{133}Cs are available in EXFOR. The number of data for ^{133}Cs is 24. The nuclides ^{153}Eu and ^{155}Gd have the same isospin values as ^{137}Cs ($N-Z = 27$). A total of 51 data points were collected. These 75 data points contribute to the calculations of ^{137}Cs . Similarly, the excitation function of ^{107}Pd (n,

Fig. 9 (Color online) (n, 2n) cross-sections for isotopes of Co, Se, Zr, Pd, Sn, and Cs. The curves represent the calculations by the tensor model, whereas the dots represent the EXFOR data



$^{2n}^{106}\text{Pd}$ shown in Fig. 8 is completed by the contributions of 93 data points of isotopes $^{102,110}\text{Pd}$ ($Z = 46$) and 77 data points of the nuclides ^{109}Ag and ^{113}In ($N - Z = 15$). The total quantity reaches 170, nearly 2.5 times larger than that for ^{137}Cs . However, as shown in Fig. 8d and f, the calculations for ^{137}Cs are more precise than those for ^{107}Pd . Note also the underestimation of the cross-sections for ^{107}Pd above 10 MeV. This is attributed to the data for ^{109}Ag in the same energy region. This indicates the significance of high-quality data for model training.

3.2 Application in selective transmutation

Disposal of radioactive nuclear waste has always been a concern. The concept of partition–transmutation provides a new approach to transform secondary actinide nuclides and LLFPs into short-lived, low radioactive, or stable nuclides by transmutation. The concept of selective transmutation was then proposed. By determining the energy regions of LLFPs, transmutation can be realized for the targeted LLFPs, which has the advantage of reducing the generation of new long-lived unstable nuclides in the process. In this study, the (n, 2n) reaction cross-sections varying with energy for LLFPs such as Co, Se, Zr, Pd, Sn, and Cs, were predicted, which provides the possibility of realizing selective transmutation.

Figure 9 shows the (n, 2n) cross-sections for the isotopes of Co, Se, Zr, Pd, Sn, and Cs. For a stable nuclide $^A X$, as the neutron number increases, the nucleus becomes

less stable, and the single-neutron separation energy tends to decrease, which corresponds to a decrease in the threshold energy of $^A X(n, 2n)^{A-1} X$. This is observed from the results for $^{74,76,78,80,82}\text{Se}$, $^{88,90,96}\text{Zr}$, $^{102,104,106,108,110}\text{Pd}$, and $^{112,114,118,120,124,126}\text{Sn}$. Note that ^{79}Se , ^{93}Zr , and $^{105,107}\text{Pd}$ are nuclides with odd numbers of neutrons and even numbers of protons, which are less stable than their even–even isotopes, and are easier to separate a neutron from the nucleus. The single-neutron separation energy is much smaller than that of even–even isotopes. This is also observed in Fig. 9a. Note that ^{60}Co ($Z = 27, N = 33$) is less stable than ^{59}Co ($Z = 27, N = 32$) owing to the odd number of neutrons. The single-neutron separation energy of ^{60}Co is smaller than that of ^{59}Co . According to Fig. 9f, for Cs with odd proton numbers and even neutron numbers, the single-neutron separation energy tends to decrease as the neutron number increases, similar to the case of stable nuclides. This tendency, which is related to the neutron number, is well-represented by the tensor model.

The thresholds for these isotopes vary, with specific reactions allowed only at energies higher than their respective thresholds. As depicted in Fig. 9a, for Co in the energy region between 8 MeV and 11 MeV, the cross-sections for ^{60}Co reach the order of a barn, whereas those for ^{59}Co remain very small, not exceeding 10^{-1} . Consequently, in this energy range, the main reaction is $^{60}\text{Co}(n, 2n)^{59}\text{Co}$, which leads to transmutation of the radioactive long-lived fission product ^{60}Co into a stable isotope ^{59}Co . Similar scenarios are observed for Se (Fig. 9b), where the radioactive isotope ^{79}Se can be transmuted into the stable isotopes

^{78}Se in the energy range between 8 MeV and 10 MeV. The same applies to ^{126}Sn , as shown in Fig. 9e, within the energy range between 9 MeV and 9.6 MeV, and to ^{137}Cs , as illustrated in Fig. 9f for energy levels between 8.8 MeV and 9.2 MeV.

Regarding Zr, Fig. 9c depicts a noteworthy phenomenon occurring in the energy region between 8 MeV and 12 MeV. Notably, in addition to ^{93}Zr , the cross-sections for ^{96}Zr are also significant. This suggests that both $^{93}\text{Zr}(n, 2n)^{92}\text{Zr}$ and $^{96}\text{Zr}(n, 2n)^{95}\text{Zr}$ reactions can occur within this energy range. Consequently, the radioactive isotope ^{93}Zr undergoes transmutation into the stable nuclide ^{92}Zr , whereas the products of $^{96}\text{Zr}(n, 2n)$ reactions are also stable isotopes that do not yield new radioactive products. A similar scenario unfolds in the case of ^{107}Pd , as shown in Fig. 9d. In the energy region between 7 MeV and 9 MeV, the radioactive isotope ^{107}Pd can be transmuted into the stable isotope ^{106}Pd , and ^{105}Pd can undergo transmutation into ^{104}Pd , which is also a stable isotope. These examples illustrate the potential for selective transmutation based on cross-sections calculated using the proposed tensor model. This capability is instrumental in efficiently managing long-lived fission products and avoiding unnecessary reactions.

4 Summary

In this study, we constructed a tensor model based on the collaborative filtering algorithm, which is a machine learning technique used in recommendation systems. The model uses tensor decomposition and completion to predict (n, 2n) reaction cross-sections, in which the EXFOR data of the (n, 2n) reaction cross-sections are applied as the training data. The calculations performed using the tensor model were compared with EXFOR data. A consistent trend was observed in the majority of cases. Statistical analysis reveals that for over 90% of the instances, the calculated results were within two times the ratio of the experimental data. This robust performance underscores the feasibility of the tensor model.

One notable contribution of the proposed tensor model is its ability to complete missing (n, 2n) reaction cross-sectional data in EXFOR. This can be explained by its collaborative filtering algorithm, which makes the model clearer than a black-box model. To validate the model, we selected nuclides with either a substantial amount of experimental data, such as ^{90}Zr , or data with significant deviations, as exemplified by ^{84}Sr . The results from these examples are reasonable and generally agree with the data from various evaluation databases. Cases where deviations

occur can often be explained. This study mainly focuses on the performance of the tensor model for the prediction of (n, 2n) reaction cross-sections and provides a preliminary reference for the database. It is important to note that the accuracy of the reproduction and data prediction depends on both the quality of the data and performance of the model. Therefore, continual improvement can be pursued, including the thoughtful selection of experimental data based on their physical relevance. A rigorous data evaluation procedure should be conducted to obtain more accurate results, which will be performed in the future studies.

The cross-sections of LLFPs are predicted using this model. The results are reasonable and agree with data from various evaluation databases. By analyzing the varying energy thresholds for (n, 2n) reactions among different isotopes of LLFPs, we identified suitable energy ranges for the transmutation of each LLFP. Within these ranges, only LLFPs with high cross-sectional values can be effectively transmuted into shorter-lived or less radioactive isotopes. This approach helps circumvent the unnecessary transmutation of stable isotopes and reduce the new generation of the long-lived radioactive nuclides to a significant extent. These findings underscore the practical application of predictions made by the tensor model, particularly in the context of nuclear waste disposal. This approach holds promise for more efficient and targeted management of nuclear waste.

Author contributions All authors contributed to the study conception and design. Material preparation, data collection, and analysis were performed by Jia-Li Huang, Hui Wang, and Jun Su. The first draft of the manuscript was written by Jia-Li Huang, and all authors commented on the previous versions of the manuscript. All authors read and approved the final manuscript.

Data availability The data that support the findings of this study are openly available in Science Data Bank at <https://cstr.cn/31253.11.sciencedb.j00186.00232> and <https://www.doi.org/10.57760/sciencedb.j00186.00232>.

Declarations

Conflict of interest The authors declare that they have no conflict of interest.

References

1. A. Kalamara, R. Vlastou, M. Kokkoris et al., $^{197}\text{Au}(n,2n)$ reaction cross section in the 15–21 MeV energy range. *Phys. Rev. C* **97**, 034615 (2018). <https://doi.org/10.1103/PhysRevC.97.034615>
2. N. Patronis, C.T. Papadopoulos, S. Galanopoulos et al., Activation cross section and isomeric cross-section ratio for the (n,2n) reaction on ^{191}Ir . *Phys. Rev. C* **75**, 034607 (2007). <https://doi.org/10.1103/PhysRevC.75.034607>
3. A. Kalamara, R. Vlastou, M. Kokkoris et al., $^{191}\text{Ir}(n,2n)$ and $^{191}\text{Ir}(n,3n)$ reaction cross sections in the 15–21 MeV energy range.

- Phys. Rev. C **98**, 034607 (2018). <https://doi.org/10.1103/PhysRevC.98.034607>
4. S. Akkoyun, N. Amrani, T. Bayram, Neural network predictions of (n,2n) reaction cross-sections at 14.6 MeV incident neutron energy. *Appl. Radiat. Isot.* **191**, 110554 (2023). <https://doi.org/10.1016/j.apradiso.2022.110554>
 5. E. Georgali, Z. Eleme, N. Patronis et al., The (n, 2n) reaction for the lightest stable erbium isotope ^{162}Er from reaction threshold up to 19 MeV. *Phys. Rev. C* **98**, 014622 (2018). <https://doi.org/10.1103/PhysRevC.98.014622>
 6. S.W. Finch, M. Bhihe, Krishichayan et al., ^{169}Tm (n,2n) ^{168}Tm and ^{169}Tm (n,3n) ^{167}Tm cross-section measurements from 15 to 21 MeV. *Phys. Rev. C* **103**, 044609 (2021). <https://doi.org/10.1103/PhysRevC.103.044609>
 7. C. Zhu, H. Guo, J. Wang et al., Measurement of ^{169}Tm (n,2n) ^{168}Tm reaction cross sections from 12 to 19.8 MeV. *Chin. Phys. C* **47**, 114101 (2023). <https://doi.org/10.1088/1674-1137/acf287>
 8. J. Soter, M. Bhihe, S.W. Finch et al., Measurements of the ^{169}Tm (n,2n) ^{168}Tm cross section from threshold to 15 MeV. *Phys. Rev. C* **96**, 064619 (2017). <https://doi.org/10.1103/PhysRevC.96.064619>
 9. S. Badwar, R. Ghosh, B.M. Lawrinang et al., Measurement of formation cross-section of ^{99}Mo from the $^{98}\text{Mo}(n,\gamma)$ and $^{100}\text{Mo}(n,2n)$ reactions. *Appl. Radiat. Isotop.* **129**, 117–123 (2017). <https://doi.org/10.1016/j.apradiso.2017.08.019>
 10. N. Shetty, R. Makwana, M. Mehta et al., Measurement of neutron induced $^{86}\text{Sr}(n, 2n)^{85}\text{Sr}$ reaction cross sections at different neutron energies. *Appl. Radiat. Isotop.* **154**, 108866 (2019). <https://doi.org/10.1016/j.apradiso.2019.108866>
 11. J. Luo, L. Jiang, L. He, Measurement of cross sections and isomeric cross-section ratios for the (n,2n) reactions on $^{196,198}\text{Hg}$ at energies between 13 and 15 MeV. *Phys. Rev. C* **98**, 014619 (2018). <https://doi.org/10.1103/PhysRevC.98.014619>
 12. T. Mori, A. Yogo, T. Hayakawa et al., Direct evaluation of high neutron density environment using (n,2n) reaction induced by laser-driven neutron source. *Phys. Rev. C* **104**, 015808 (2021). <https://doi.org/10.1103/PhysRevC.104.015808>
 13. A. Kalamara, R. Vlastou, M. Kokkoris et al., Investigation of the $^{241}\text{Am}(n,2n)^{240}\text{Am}$ cross section. *Phys. Rev. C* **93**, 014610 (2016). <https://doi.org/10.1103/PhysRevC.93.014610>
 14. V. Méot, O. Roig, B. Laurent et al., $^{239}\text{Pu}(n, 2n)^{238}\text{Pu}$ cross section measurement using a recoil method. *Phys. Rev. C* **103**, 054609 (2021). <https://doi.org/10.1103/PhysRevC.103.054609>
 15. T. Ganesapandy, J. Jeremiah, S. Dahiwalé et al., Analysis of neutron induced (n, γ) and (n,2n) reactions on ^{232}Th from reaction threshold to 20 MeV. *Appl. Radiat. Isotop.* **150**, 70–78 (2019). <https://doi.org/10.1016/j.apradiso.2019.05.021>
 16. U.E. Humphrey, M.U. Khandaker, Viability of thorium-based nuclear fuel cycle for the next generation nuclear reactor: issues and prospects. *Renew. Sustain. Energy Rev.* **97**, 259–275 (2018). <https://doi.org/10.1016/j.rser.2018.08.019>
 17. Z. Liu, C. Yang, Y. Yang et al., Measurement and analysis of $^{232}\text{Th}(n,2n)^{231}\text{Th}$ reaction rate in the thorium oxide cylinder with a D-T neutron source. *Ann. Nucl. Energy* **111**, 660–665 (2018). <https://doi.org/10.1016/j.anucene.2017.06.041>
 18. X.Y. Sun, W. Luo, H.Y. Lan et al., Transmutation of long-lived fission products in an advanced nuclear energy system. *Sci. Rep.* **12**, 2240 (2022). <https://doi.org/10.1038/s41598-022-06344-y>
 19. S. Kunieda, N. Furutachi, F. Minato et al., JENDL/ImPACT-2018: a new nuclear data library for innovative studies on transmutation of long-lived fission products. *J. Nucl. Sci. Technol.* **56**, 1073–1091 (2019). <https://doi.org/10.1080/00223131.2019.1647889>
 20. T. Hayakawa, S. Miyamoto, R. Hajima et al., Proposal for selective isotope transmutation of long-lived fission products using quasi-monochromatic γ -ray beams. *J. Nucl. Sci. Technol.* **53**, 2064–2071 (2016). <https://doi.org/10.1080/00223131.2016.1194776>
 21. V. Apse, G. Kulikov, E. Kulikov, Role of (n2n) reactions in transmutation of long-lived fission products. *Phys. Atom. Nucl.* **79**, 1513–1518 (2016). <https://doi.org/10.1134/S1063778816130019>
 22. M. Igashira, T. Ohsaki, Neutron economy and nuclear data for transmutation of long-lived fission products. *Prog. Nucl. Energ.* **40**, 555–560 (2002). [https://doi.org/10.1016/S0149-1970\(02\)00050-1](https://doi.org/10.1016/S0149-1970(02)00050-1)
 23. Z.L. Zhao, Y.W. Yang, H.Y. Meng et al., Preparation and verification of mixed high-energy neutron cross-section library for ads. *Nucl. Sci. Tech.* **29**, 140 (2018). <https://doi.org/10.1007/s41365-018-0487-9>
 24. Q. Liu, N. Ofoq, M. Jing et al., (2023) Determination of cross-sections of $^{nat}\text{Pb}(p, x)^{207}\text{Bi}$ and $^{nat}\text{Pb}(p, x)^{194}\text{Hg}$ by gethu. *Nuclear Techniques (in Chinese)* **46**, 090501. <https://doi.org/10.11889/j.0253-3219.2023.hjs.46.090501>
 25. J. Chen, X. Chen, X. Ruan et al., A new neutron detector designed for (n,2n) and (n,3n) reaction cross section measurements. *Nucl. Instrum. Methods Phys. Res. Sect. A* **910**, 157–163 (2018). <https://doi.org/10.1016/J.NIMA.2018.09.020>
 26. A.C. Larsen, A. Spyrou, S.N. Liddick et al., Novel techniques for constraining neutron-capture rates relevant for r-process heavy-element nucleosynthesis. *Prog. Part. Nucl. Phys.* **107**, 69–108 (2019). <https://doi.org/10.1016/j.ppnp.2019.04.002>
 27. O.C. Gorton, J.E. Escher, Cross sections for neutron-induced reactions from surrogate data: reexamining the Weisskopf-ewing approximation for (n, n') and (n,2n) reactions. *Phys. Rev. C* **107**, 044612 (2023). <https://doi.org/10.1103/PhysRevC.107.044612>
 28. A. Koning, Statistical verification and validation of the exfor data base:(n,n'),(n,2n),(n,p),(n, α) and other neutron-induced threshold reaction cross-sections. Organisation for Economic Co-Operation and Development **NEA-DB-DOC-2014-3**,
 29. X. Dong, L. Geng, Machine learning method in study of nuclear charge radius. *At. Energy Sci. Technol. (in Chinese)* **57**, 679 (2023). <https://doi.org/10.7538/yzk.2022.youxian.0859>
 30. J. Li, T. Zhao, N. Ma et al., Application of neural network approach in nuclear mass. *At. Energy Sci. Technol. (in Chinese)* **57**, 696 (2023). <https://doi.org/10.7538/yzk.2022.youxian.0778>
 31. X.C. Ming, H.F. Zhang, R.R. Xu et al., Nuclear mass based on the multi-task learning neural network method. *Nucl. Sci. Tech.* **33**, 48 (2022). <https://doi.org/10.1007/s41365-022-01031-z>
 32. Z.P. Gao, Y.J. Wang, H.L. Lü et al., Machine learning the nuclear mass. *Nucl. Sci. Tech.* **32**, 109 (2021). <https://doi.org/10.1007/s41365-021-00956-1>
 33. Y. Tian, R. Xu, X. Tao et al., Analyzing fission cross section of u isotope by neural network method. *At. Energy Sci. Technol. (in Chinese)* **57**, 805 (2023). <https://doi.org/10.7538/yzk.2023.youxian.0048>
 34. C.W. Ma, X.B. Wei, X.X. Chen et al., Precise machine learning models for fragment production in projectile fragmentation reactions using Bayesian neural networks *. *Chin. Phys. C* **46**, 074104 (2022). <https://doi.org/10.1088/1674-1137/ac5efb>
 35. Q.F. Song, L. Zhu, J. Su, Target dependence of isotopic cross sections in the spallation reactions $^{238}\text{U} + p, d$ and ^9Be at 1 A GeV*. *Chin. Phys. C* **46**, 074108 (2022). <https://doi.org/10.1088/1674-1137/ac6249>
 36. Y. Wang, Q. Li, Machine learning transforms the inference of the nuclear equation of state. *Front. Phys-Beijing* **18**, 64402 (2023). <https://doi.org/10.1007/s11467-023-1313-3>
 37. Y. Wang, F. Li, Q. Li et al., Finding signatures of the nuclear symmetry energy in heavy-ion collisions with deep learning. *Phys. Lett. B* **822**, 136669 (2021). <https://doi.org/10.1016/j.physletb.2021.136669>
 38. Y. Wang, Z. Gao, H. Lü et al., Decoding the nuclear symmetry energy event-by-event in heavy-ion collisions with machine

- learning. *Phys. Lett. B* **835**, 137508 (2022). <https://doi.org/10.1016/j.physletb.2022.137508>
39. P. Vicente-Valdez, L. Bernstein, M. Fratoni, Nuclear data evaluation augmented by machine learning. *Ann. Nucl. Energy* **163**, 108596 (2021). <https://doi.org/10.1016/j.anucene.2021.108596>
 40. D. Neudecker, M. Grosskopf, M. Herman et al., Enhancing nuclear data validation analysis by using machine learning. *Nucl. Data Sheets* **167**, 36–60 (2020). <https://doi.org/10.1016/j.nds.2020.07.002>
 41. W. He, Q. Li, Y. Ma et al., Machine learning in nuclear physics at low and intermediate energies. *Sci. China Phys. Mech. Astron.* **66**, 282001 (2023). <https://doi.org/10.1007/s11433-023-2116-0>
 42. X. Sun, Z. Wei, D. Wang et al., Study of (n, 2n) reaction cross section of fission product based on neural network and decision tree model. *EPJ Web of Conferences* **294**, 04008 (2024). <https://doi.org/10.1051/epjconf/202429404008>
 43. Q. Song, L. Zhu, B. Cai et al., Image processing of isotope yield in neutron-induced fission. *Phys. Rev. C* **107**, 044609 (2023). <https://doi.org/10.1103/physrevc.107.044609>
 44. Q.F. Song, L. Zhu, H. Guo et al., Verification of neutron-induced fission product yields evaluated by a tensor decomposition model in transport-burnup simulations. *Nucl. Sci. Tech.* **34**, 32 (2023). <https://doi.org/10.1007/s41365-023-01176-5>
 45. H. Wang, J. Huang, J. Su, Studying differential cross section for elastic proton scattering by a tensor model. *Prog. Nucl. Energy* **165**, 104891 (2023). <https://doi.org/10.1016/j.pnucene.2023.104891>
 46. J. Liu, P. Musialski, P. Wonka et al., Tensor completion for estimating missing values in visual data. *IEEE Trans. Pattern Anal. Mach. Intell.* **35**, 208–220 (2013). <https://doi.org/10.1109/TPAMI.2012.39>
 47. X. Chen, Z. He, L. Sun, A Bayesian tensor decomposition approach for spatiotemporal traffic data imputation. *Transport. Res. C-Emer. Technol.* **98**, 73–84 (2019). <https://doi.org/10.1016/j.trc.2018.11.003>
 48. X. Chen, Z. Han, Y. Wang et al., A general model for robust tensor factorization with unknown noise. arXiv preprint [arXiv:1705.06755](https://arxiv.org/abs/1705.06755)
 49. R. Salakhutdinov, A. Mnih, in *Proceedings of the 25th international conference on Machine learning*, Bayesian probabilistic matrix factorization using markov chain monte carlo. 2008, pp. 880–887. <https://doi.org/10.1145/1390156.1390267>
 50. L. Xiong, X. Chen, T.K. Huang et al., in *Proceedings of the 2010 SIAM international conference on data mining*, Temporal collaborative filtering with bayesian probabilistic tensor factorization. SIAM, 2010, pp. 211–222. <https://doi.org/10.1137/1.9781611972801.19>
 51. X. Chen, L. Sun, Bayesian temporal factorization for multidimensional time series prediction. *IEEE T. Pattern Anal. Mach. Intell.* **44**, 4659–4673 (2021). <https://doi.org/10.1109/TPAMI.2021.3066551>
 52. X. Wang, L. Zhu, J. Su, Modeling complex networks of nuclear reaction data for probing their discovery processes. *Chin. Phys. C* **45**, 124103 (2021). <https://doi.org/10.1088/1674-1137/ac23d5>
- Springer Nature or its licensor (e.g. a society or other partner) holds exclusive rights to this article under a publishing agreement with the author(s) or other rightsholder(s); author self-archiving of the accepted manuscript version of this article is solely governed by the terms of such publishing agreement and applicable law.